



**HAL**  
open science

## Correlating chemical and electronic states from quantitative photoemission electron microscopy of transition-metal dichalcogenide heterostructures

Olivier Renault, Hokwon Kim, Dumitru Dumcenco, Dmitrii Unuchek, Nicolas Chevalier, Maxime Gay, Andras Kis, Neal Fairley

► **To cite this version:**

Olivier Renault, Hokwon Kim, Dumitru Dumcenco, Dmitrii Unuchek, Nicolas Chevalier, et al.. Correlating chemical and electronic states from quantitative photoemission electron microscopy of transition-metal dichalcogenide heterostructures. *Journal of Vacuum Science & Technology A*, 2021, 39 (5), pp.053210. 10.1116/6.0001135 . cea-04903831

**HAL Id: cea-04903831**

**<https://cea.hal.science/cea-04903831v1>**

Submitted on 21 Jan 2025

**HAL** is a multi-disciplinary open access archive for the deposit and dissemination of scientific research documents, whether they are published or not. The documents may come from teaching and research institutions in France or abroad, or from public or private research centers.





L'archive ouverte pluridisciplinaire **HAL**, est destinée au dépôt et à la diffusion de documents scientifiques de niveau recherche, publiés ou non, émanant des établissements d'enseignement et de recherche français ou étrangers, des laboratoires publics ou privés.



RESEARCH ARTICLE | AUGUST 18 2021

## Correlating chemical and electronic states from quantitative photoemission electron microscopy of transition-metal dichalcogenide heterostructures

Special Collection: [Commemorating the Career of Charles S. Fadley](#)

Olivier Renault   ; Hokwon Kim  ; Dumitru Dumcenco; Dmitrii Unuchek; Nicolas Chevalier  ; Maxime Gay; Andras Kis  ; Neal Fairley



*J. Vac. Sci. Technol. A* 39, 053210 (2021)

<https://doi.org/10.1116/6.0001135>



### Articles You May Be Interested In

Noble-transition-metal dichalcogenides-emerging two-dimensional materials for sensor applications

*Appl. Phys. Rev.* (July 2023)

Ultrafast exciton relaxation in monolayer transition metal dichalcogenides

*J. Appl. Phys.* (April 2016)

Interlayer registry effects on the electronic and piezoelectric properties of transition metal dichalcogenide bilayers

*J. Vac. Sci. Technol. A* (March 2024)



Advance your science and  
career as a member of

**AVS**

LEARN MORE



# Correlating chemical and electronic states from quantitative photoemission electron microscopy of transition-metal dichalcogenide heterostructures

Cite as: J. Vac. Sci. Technol. A 39, 053210 (2021); doi: 10.1116/6.0001135

Submitted: 10 May 2021 · Accepted: 19 July 2021 ·

Published Online: 18 August 2021



View Online



Export Citation



CrossMark

Olivier Renault,<sup>1,a)</sup> Hokwon Kim,<sup>2,b)</sup> Dumitru Dumcenco,<sup>2</sup> Dmitrii Unuchek,<sup>2</sup> Nicolas Chevalier,<sup>1</sup> Maxime Gay,<sup>1</sup> Andras Kis,<sup>2</sup> and Neal Fairley<sup>3</sup>

## AFFILIATIONS

<sup>1</sup>Univ. Grenoble Alpes, CEA, Leti, F-38000 Grenoble, France

<sup>2</sup>Electrical Engineering Institute, École Polytechnique Fédérale de Lausanne (EPFL), CH-1015 Lausanne, Switzerland

<sup>3</sup>Casa Software Ltd, Bay House, 5 Grosvenor Terrace, Teignmouth, Devon TQ14 8NE, United Kingdom

**Note:** This paper is a part of the Special Collection Commemorating the Career of Charles S. Fadley.

**a) Author to whom correspondence should be addressed:** [olivier.renault@cea.fr](mailto:olivier.renault@cea.fr)

**b) Present address:** Hauptstrasse 1A, 9477 Trübbach, Switzerland.

## ABSTRACT

Vertical heterostructures of MoS<sub>2</sub> and WSe<sub>2</sub> layers are studied by spectroscopic photoemission electron microscopy as an effective technique for correlating chemical and electronic states at the micrometer scale. Element-specific, surface-sensitive images recorded at high lateral and energy resolution from core-level photoelectrons using different laboratory excitation sources are postprocessed to obtain laterally resolved maps of elemental composition and energy shifts in the Mo3d spectra of a few hundred meV. For monolayer MoS<sub>2</sub>, the method reveals substrate-dependent charge transfer properties within the narrow energy range of 360 meV, with MoS<sub>2</sub> becoming more *n*-type after transfer onto WSe<sub>2</sub>. The band structure data from momentum microscopy taken over the same areas confirm the charge transfer from WSe<sub>2</sub> to MoS<sub>2</sub> by the shift of the K-bands away from the Fermi level and illustrates the layer-specific contributions to the electronic band structure of the heterostructure. From work function mapping, the reconstructed energy-level diagram reveals a type II heterostructure but with a very small conduction-band offset.

Published under an exclusive license by the AVS. <https://doi.org/10.1116/6.0001135>

## I. INTRODUCTION

With the advent of few-layer transition metal dichalcogenide (TMD) MX<sub>2</sub> materials (M = Mo, W, Re, ...; X = S, Se, Te, ...) exhibiting novel physical properties of interest for a wide range of applications, there is a pressing need for novel analytical methods to be efficiently implemented at conventional surface-sensitive microscopic techniques such as x-ray photoelectron spectroscopy (XPS) or angle-resolved photoemission spectroscopy (ARPES). XPS and by extension photoelectron spectroscopy using synchrotron radiation have long been the techniques of choice for unraveling chemical and electronic properties of surfaces and are,

therefore, extremely well suited for studying TMD materials. Synchrotron-based techniques for photoemission microscopy are powerful both in scanning and full-field modes,<sup>1</sup> because bright tunable excitation sources are employed, therefore, allowing analyses at higher resolutions (both laterally and energetically speaking) than with laboratory instruments. However, quantification is always an issue due to imperfect instrument characterization and photon flux variability. Bright photon sources may also induce beam effects on delicate TMD materials, as reported many times on multiple systems.<sup>2</sup> It is, therefore, desirable for laboratory-based microscopy techniques to image TMDs' surface properties. Only photoemission

electron microscopy (PEEM)-based instruments have demonstrated resolutions high enough to tackle the challenge of TMD characterization, requiring investigations at the low-micrometer scale. However, to date, although 2D materials were already analyzed using XPEEM and micrometer-scale ARPES,<sup>1,3–6</sup> no proper quantification approach was setup and critically assessed. Moreover, the demonstration of sound correlation of chemical and electronic properties is still scarce<sup>3,5,7</sup> and only performed with synchrotron radiation, often employing the absorption channel for elemental fingerprinting. Despite the much lower photon flux of laboratory x-ray sources compared to synchrotron-based ones, it has been demonstrated in the past that core-level imaging was effective, keeping in mind, of course, the longer acquisition time.<sup>8,9</sup> Here, we demonstrate the first example of quantitative elemental and chemical photoelectron microscopy at the micrometer scale together with correlations to the corresponding band structure measured on the same area using a lab-scale photoemission electron microscope.

## II. EXPERIMENT

### A. CVD of layered transition metal dichalcogenide and vertical heterostructure fabrication

The MoS<sub>2</sub> and WSe<sub>2</sub> layers were synthesized separately by metal-organic vapor deposition and chemical vapor deposition, respectively, where the details of the methods are published previously elsewhere.<sup>10,11</sup> Briefly, Mo(CO)<sub>6</sub> and H<sub>2</sub>S were used as Mo and S sources, respectively, at the growth temperature of 950 °C with 10 μg of KI, which acts as the 2D growth promoter, placed in front of the substrates. For WSe<sub>2</sub> growth, WO<sub>3</sub> and Se powder sources were used. Following the method outlined by Li *et al.*,<sup>12</sup> we added a small amount of NaCl to the WO<sub>3</sub> source in order to enhance the W evaporation and improve the morphology and the coverage of WSe<sub>2</sub> on the sapphire substrates.

### B. Transfer of individual TMDs for vertical heterostructure fabrication

The as-grown WSe<sub>2</sub> and MoS<sub>2</sub> islands on sapphire were transferred sequentially onto a 1 × 1 cm<sup>2</sup> conductive, p-type Si substrate with a native oxide to create the MoS<sub>2</sub>/WSe<sub>2</sub>/SiO<sub>2</sub>/Si vertical heterostructure (VHS) using a deterministic, semidry transfer method described in detail elsewhere.<sup>10,13</sup> In short, CVD-grown WSe<sub>2</sub> was individually coated with PMMA and attached to a Polydimethylsiloxane (PDMS) stamp. The sapphire/2D material/PMMA/PDMS stack was immersed in a warm KOH solution bath (15 wt. %) for 20 min, rinsed in DI water several times, and the sapphire substrate was detached. The WSe<sub>2</sub>/PMMA/PDMS stack was mounted and positioned on a custom-made stage loaded with a target silicon substrate to carefully align and position the stack with respect to the target substrate by means of optical microscope and gently brought into contact with the surface of the substrate. After heating the substrate at 100 °C for 30 min in order to improve the adhesion, the PMMA/PDMS stamps were removed by immersing in an acetone bath and the WSe<sub>2</sub>/Si sample was cleaned and dried. Similarly, MOCVD-MoS<sub>2</sub> islands on sapphire<sup>11</sup> were deterministically

transferred to the WSe<sub>2</sub> island area on the WSe<sub>2</sub>/Si sample in order to create the sandwiched VHS. The VHS were finally annealed in an Ar/H<sub>2</sub> environment for removal of residual PMMA.

### C. Photoemission electron microscopy

Core-level spectroscopic imaging was performed using a NanoESCA MkI XPEEM (Scienta Omicron) described previously elsewhere.<sup>14,15</sup> Prior to imaging, the sample was annealed in an ultrahigh vacuum ambient (base pressure  $5 \times 10^{-11}$  mbar) at 350 °C for 1 h to remove adventitious carbon contamination. Navigation was performed by recording live, secondary-electron images produced by a mercury arc source (5.2 eV). Core-level spectroscopic images were acquired with a monochromated, microfocussed Al K $\alpha$  source providing a typical photon flux of  $5 \times 10^{12}$  ph/s within a spot size of 150 μm. The microscope settings were adjusted to yield an overall energy resolution (photon bandwidth and spectrometer broadening) of 0.47 eV at an instrumental lateral resolution of 500 nm, achieved with a spectrometer pass energy/entrance slit of 50 eV/2 mm and a 500 μm diameter contrast aperture, respectively. Here, we have implemented pulse-counting, two-dimensional image detection with a single event algorithm, which essentially enables us to lower the noise level from 100 gray scales in a conventional multichannel plate-based setup down to virtually zero.<sup>16</sup> This is a prerequisite not only to push up the sensitivity necessary when imaging atomically thin materials, but more importantly for image quantification purposes requesting linear dependency of the intensity. The typical acquisition conditions of the core-level images were chosen so as to provide meaningful data sets for the quantitative analysis, bearing in mind the atomically thin materials analyzed here; therefore, we deliberately maximized the parameters governing both the final intensity (acquisition time per image and number of scans) and the spectral resolution (number of images per electron volt). This resulted in 10 h acquisition time for Se3d and W4f images and an overall measurement time of about 60 h for the six recorded core levels (W4f, Se3d, S2p, Mo3d, Si2p, and O1s). Clearly, the acquisition time value represents an upper limit in laboratory core-level imaging, partly because of the atomically thin character of materials investigated here. To bring a complementary picture to the chemical information, the local electronic properties were studied by measuring the work function (WF) and the band structure over the same areas from direct-space, energy-filtered secondary-electron PEEM images and reciprocal-space, spectroscopic momentum microscopy of valence electrons (kPEEM). For this, an He I cold cathode lamp ( $h\nu = 21.2$  eV) was used as excitation source impinging the sample in an off-normal direction (65° with respect to the sample normal), providing the necessary intensity at the  $\Gamma$  point.<sup>17</sup> The so-called kPEEM, momentum-resolved images were acquired over the full first Brillouin zone ( $\pm 3.4 \text{ \AA}^{-1}$ ) over an energy range of 10 eV below the Fermi level. The high energy resolution momentum images were recorded at a spectrometer pass energy of 50 eV and a 1 mm diameter entrance slit of the imaging spectrometer (equivalent to an overall energy resolution of  $\sim 0.2$  eV). The k-space scale was calibrated by measuring the known reciprocal lattice distances of a

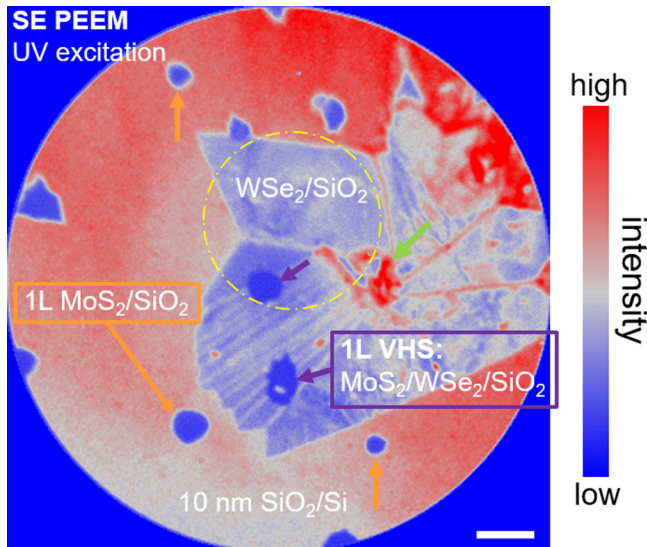


**FIG. 1.** PEEM image of the  $\text{WSe}_2$  crystal and vertical  $\text{MoS}_2/\text{WSe}_2$  heterostructures (VHS). Scale bar:  $10\ \mu\text{m}$ . Excitation: mercury arc source ( $h\nu = 5.2\ \text{eV}$ ). The yellow dashed circled area corresponds to the work function map of Fig. 6.

freshly prepared Cu (111) single crystal surface. After applying a flat-field procedure for correcting detector imperfections, the second derivative of each image series was taken to enhance the contrast of the band dispersion.

### III. RESULTS AND DISCUSSION

#### A. Domain identification and lateral resolution

Figure 1 shows an energy-filtered PEEM image at the photoemission threshold (secondary electrons) of the  $\text{WSe}_2$  crystal investigated in the following. Here, in the case of atomically thin materials presenting limited surface topography, the image contrast arises mostly from work function differences within the field of view. Besides the  $\text{SiO}_2$  substrate and the  $\text{WSe}_2$  crystal showing up, respectively, in high and low intensity scale, the darker patches of about  $10\ \mu\text{m}$  size are visible on both the substrate (orange arrow) and the  $\text{WSe}_2$  area (purple arrow). These latter regions are related to, respectively, monolayer (ML)  $\text{MoS}_2$  and VHS  $\text{MoS}_2/\text{WSe}_2$  domains, as shown below from spectroscopic data. The PEEM image also reveals heterogeneities within the crystal in the form of defects to its lower left part. Figure 2 presents the raw core-level images acquired across the  $\text{Mo}3d$  (224.5–234.5 eV),  $\text{S}2p$  (158.5–168.5 eV),  $\text{Se}3d$  (52.5–58.5 eV),  $\text{W}4f$  (30.5–36.5 eV),  $\text{O}1s$  (528.5–538.5 eV), and  $\text{Si}2p$  (98.5–105.5 eV) transitions. From a qualitative point of view, all features of interest are identified on these images, especially the monolayer  $\text{MoS}_2$  and the VHS domains as seen from the PEEM image of Fig. 1, marked with orange and purple arrows, respectively. Both  $\text{Mo}3d$  and  $\text{S}2p$  images are misleading regarding the contrast in the  $\text{WSe}_2$  area, because of line overlaps with, respectively,  $\text{Se}3s$  and  $\text{Se}3p$  core-level transitions. The green arrow in both  $\text{W}4f$  and  $\text{Se}3d$  images at the center of the crystal highlights multilayer  $\text{WSe}_2$  as frequently encountered in CVD-grown crystals. This explains why the same feature is seen in both the  $\text{Mo}3d$  and  $\text{S}2p$  images as the result of the spectral intermixing with Se lines mentioned above.

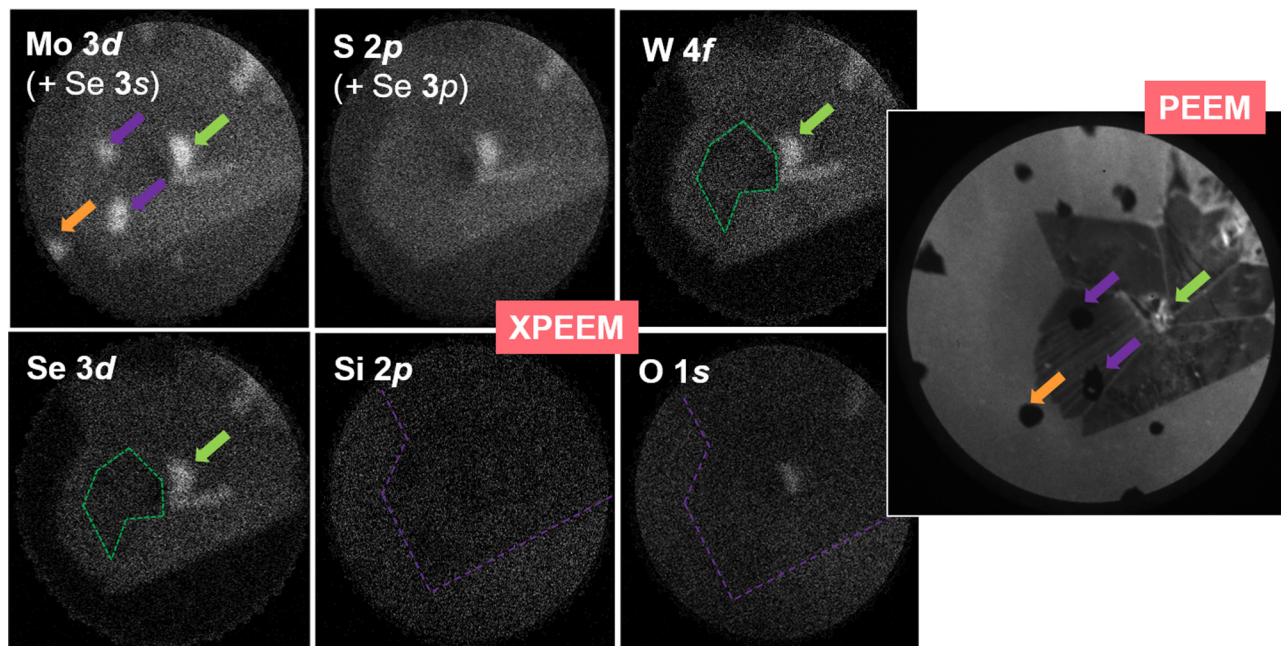


**FIG. 2.** Raw XPEEM core-level images of the  $\text{WSe}_2$  crystal and vertical  $\text{MoS}_2/\text{WSe}_2$  heterostructures (integrated intensity). Field of view of the core-level images:  $84\ \mu\text{m}$ .

21 January 2025 15:25:16

There are other interesting features contained in these raw images. First, we observe a significant contrast both in Si2p and O1s images. Although weak [we measure after applying a mean filter to the raw Si2p image a contrast ratio  $C = 1 - (I_{SiO_2} - I_{WSe_2}) / (I_{SiO_2} + I_{WSe_2})$  of 0.06], the contrast is large enough to fingerprint the coverage of the substrate by the ML-thick WSe<sub>2</sub> crystal. Here, Si2p intensities  $I_{WSe_2}$  (inside the WSe<sub>2</sub> crystal) and  $I_{SiO_2}$  (outside the WSe<sub>2</sub> crystal, on the substrate) are integrated over typically  $10 \times 10 \mu\text{m}^2$ , and it is found that the attenuation of the Si2p signal in the WSe<sub>2</sub> region is 32%. This confirms the ML-thick character of the WSe<sub>2</sub> crystal. Second, we have determined the lateral resolution of the XPEEM images in order to compare with the case of imaging of bulk materials. The contrast aperture in the PEEM column used during the experiment was  $500 \mu\text{m}$  in diameter, which corresponds approximately to an instrumental resolution of  $0.5 \mu\text{m}$ , reachable only in the case of atomically sharp interfaces of materials<sup>9</sup> with no topography whatsoever

(both roughness and nonuniformities of the surface potential will indeed deteriorate the effective lateral resolution).<sup>18</sup> Thus, we expect in practice a lateral resolution figure more around  $1 \mu\text{m}$ . The measurements were performed on the W4f and Se3d XPEEM images and are shown in Fig. 3. The calculation is performed from the distance over which the intensity profile spreads between 20% and 80% of the maximum intensity.<sup>9,19</sup> The result is  $1.7 \pm 0.4$  and  $1.5 \pm 0.6 \mu\text{m}$ , respectively, for the W4f and Se3d images, confirming the expected experimental lateral resolution. This figure is in agreement with previously published data on bulk samples.<sup>20</sup> The discrepancy between the instrumental and the experimental resolutions is explained by the heterogeneous character of the border between the WSe<sub>2</sub> crystal and the SiO<sub>2</sub> substrate, due to work function differences resulting in stray lateral electric fields perturbing the photoelectron trajectories on their way to the PEEM objective lens.<sup>18</sup> In summary, the raw core-level XPEEM images of Fig. 2 demonstrate the high sensitivity of the present XPS imaging

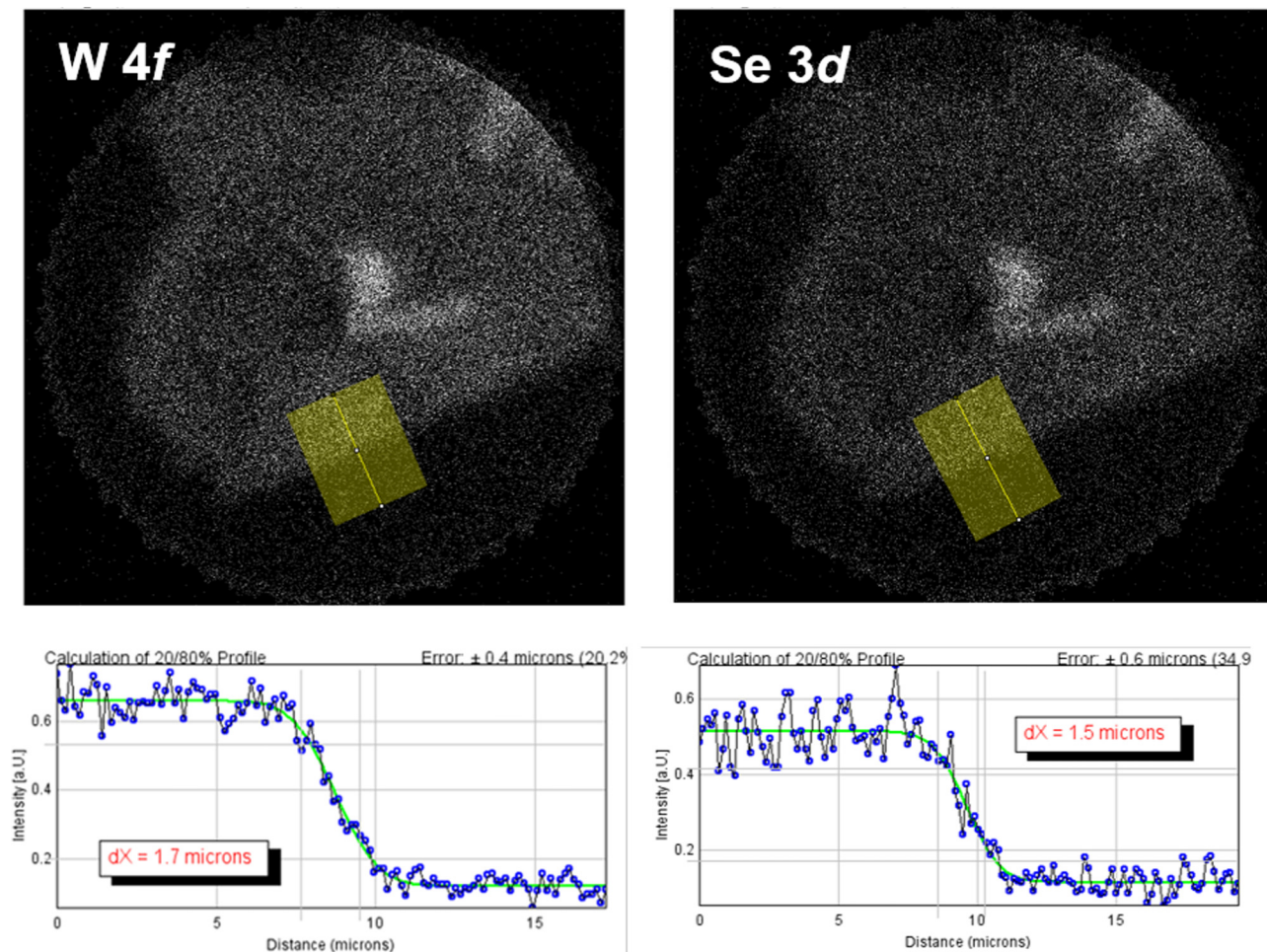


FIG. 3. Lateral resolution measurements from the raw core-level XPEEM images. Image field of view:  $84 \mu\text{m}$ .

21 January 2025 15:25:16

experiment, which displays contrasts between atomically thin domains at a measured lateral resolution of  $1\ \mu\text{m}$ .

### B. Quantitative elemental mapping

In Fig. 2, we have mentioned previously the spectral intermixing that prevents from obtaining elemental-specific Mo and S images. Also, there is a need to produce quantitative atomic concentration maps, which would enable us to determine precisely at the submicrometer scale how chemically uniform the  $\text{WSe}_2$  crystal is. To this end, we performed image processing to the data sets of Fig. 2 by applying, first, principal component analysis (PCA) to the 327 680 spectra-at-pixels in each core-level data set. Then, we attempted to generate atomic concentration images by applying Scofield cross sections and angular distribution correction based on a  $78^\circ$  angle between the x-ray source and the PEEM column. We have also considered an instrumental response to the variation in  $(E_K)^{0.9}$ , following a recent work.<sup>21</sup> For W4f, Se3d, Mo3d, and S2s, we have also applied escape depth corrections of the attenuation length assuming a thin film approximation rather than correcting for bulk material escape depth correction. The validity of these

assumptions could be checked in two ways: first, considering the atomic concentration maps of the  $\text{SiO}_2/\text{Si}$  substrate [Fig. 4(a)] and looking at the quantification of the thin oxide overlayer—a 2:1 oxygen-to-silicon ratio is found, as expected for silicon dioxide. Second, we have looked at the relative atomic concentrations of the three available Se lines distributed over a significantly large energy range (not shown)—Se3d [binding energy (BE) = 54.80 eV], Se3p<sub>3/2</sub> (BE = 161.0 eV), and Se3s (BE = 229.8 eV) to be, respectively, 33.0%, 33.54%, and 33.45%, that is, a nearly perfect 1/3 proportion, as expected. These two findings motivated us to have a closer look at the quantification of the other images. Considering first the Se and W images [Fig. 4(b)], a Se/W ratio of 2.29–2.44 can be determined in first approximation; therefore, the  $\text{WSe}_2$  crystal is Se enriched. The images also show heterogeneities in the atomic concentrations within the  $\text{WSe}_2$  crystal, starting from the V-shaped, multilayer domain at the center mentioned previously and which appears to be strongly Se enriched.

From the Si2p image presenting zero Si intensity where the V-shaped defect is sitting, it can be inferred, based on the inelastic mean-free path (IMFP) in bulk  $\text{WSe}_2$  (TPP-2M formula<sup>22</sup>) that the thickness of this structure is at least 6.4 nm. As seen from the Si2p

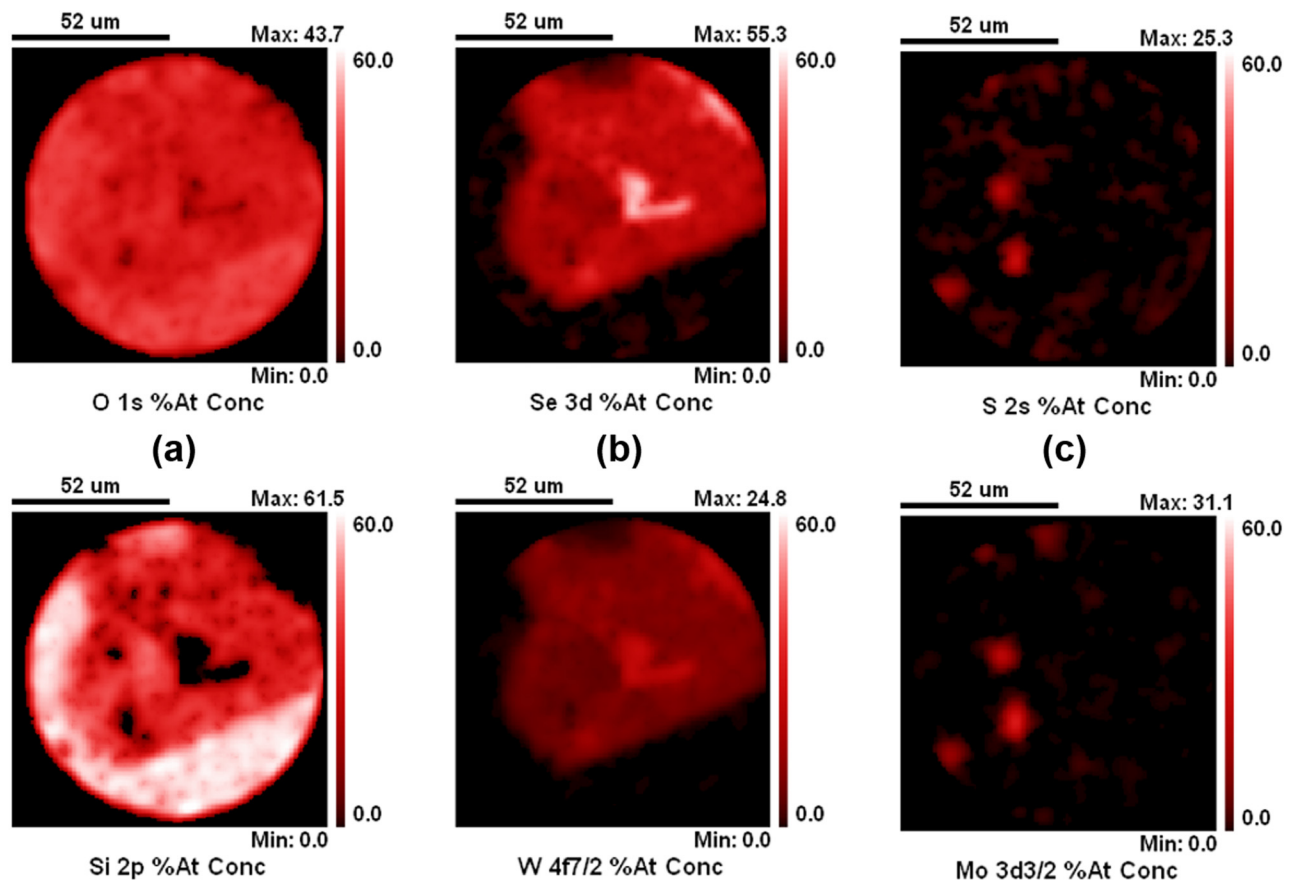
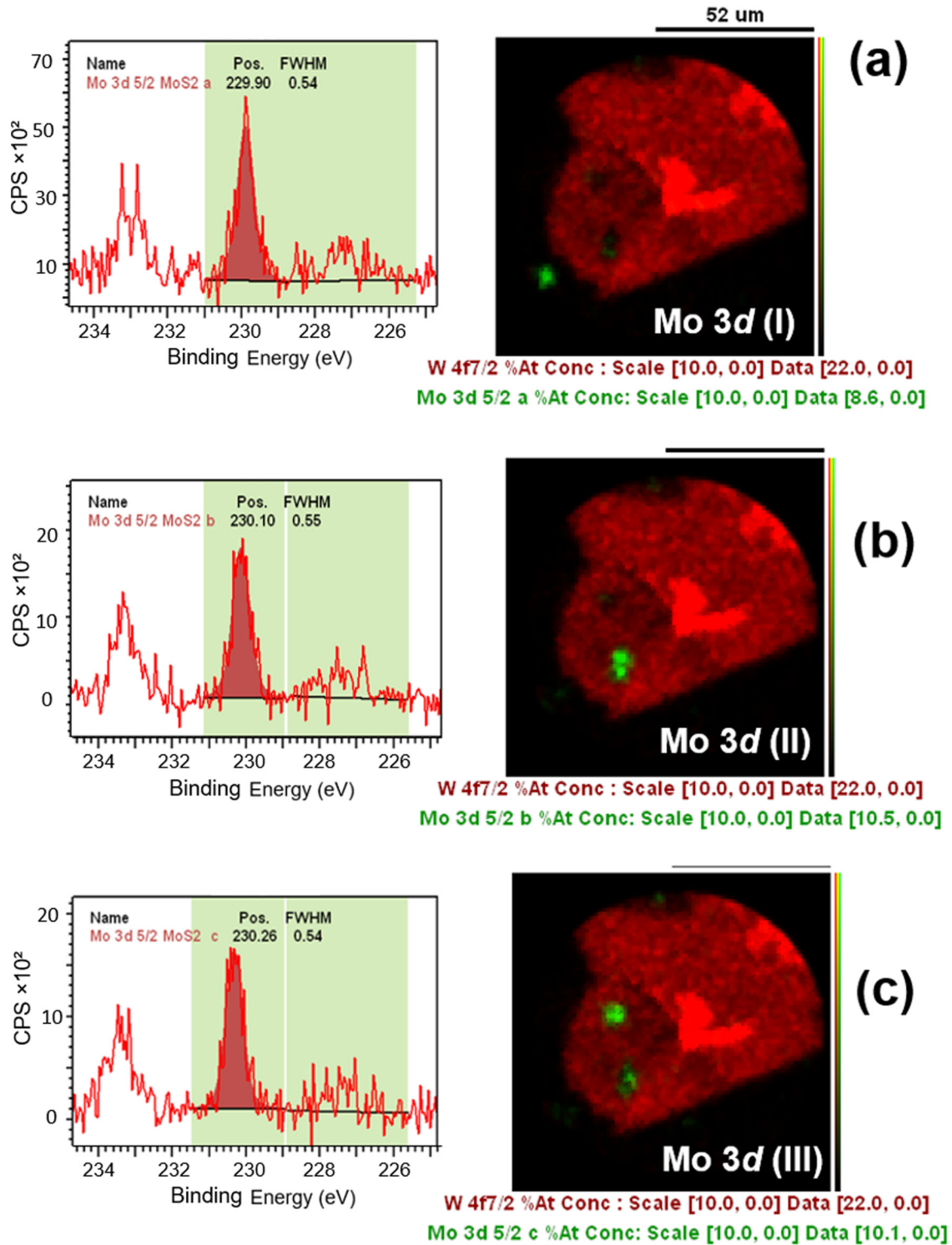


FIG. 4. PCA-enhanced elemental images of (a) the substrate, (b) the  $\text{WSe}_2$  crystal, and (c) the  $\text{MoS}_2$  domains.

21 January 2025 15:25:16



21 January 2025 15:25:16

**FIG. 5.** Chemical-state specific Mo3d images (green) from LLS decomposition of the spectra-at-pixels, superimposed on W4f elemental images: (a) Domain I, MoS<sub>2</sub>/SiO<sub>2</sub>/Si; (b) Domain II, VHS; (c) Domain III, VHS.



**TABLE I.** Mo3d<sub>5/2</sub> binding energy measured on the different domains including the vertical MoS<sub>2</sub>/WSe<sub>2</sub> heterostructures (VHS).

Domain	I	II	III	Reference
Assignment	MoS <sub>2</sub> /SiO <sub>2</sub> /Si	VHS-1	VHS-2	Bulk MoS <sub>2</sub>
BE (eV)	229.90	230.10	230.26	229.70

image, this type of thick structure is not the only one at the crystal surface: some are similar thick WSe<sub>2</sub> domains (top left of the V-shaped defect); others are the vertical MoS<sub>2</sub>/WSe<sub>2</sub> heterostructures, as confirmed in the Mo and S images. The thickness of these latter, again, exceeds 7.5 nm based on the IMFP of Si2p photoelectrons in MoS<sub>2</sub>. From the Mo and S images [Fig. 4(c)], it was found from different peak models that a reliable stoichiometry determination of the MoS<sub>2</sub> domains was difficult given the low intensity of the S2s peak. In summary, we have set up a quantification method allowing us to obtain reliable quantitative elemental XPEEM images of the TMD domains and related VHS. This procedure enables a sensitivity to defects down the low-micrometer scale.

### C. Quantitative chemical-state mapping

In order to further analyze the XPEEM images, we have generated chemical-state specific Mo 3d images in an attempt to examine substrate-dependent charge transfer behavior in MoS<sub>2</sub>. For this, we have produced images from linear-least-square (LLS) decomposition of the spectra-at-pixels of the Mo3d data set. This allows, on the one hand, subtracting the contribution from the Se3s component of the Mo3d spectra. On the other hand, the spectra-at-pixels can be partitioned according to the binding energy of the Mo3d nanospectra. In this way, we were able to divide the spectra-at-pixels in three distinct groups with binding energies detailed in Table I. The first group (Mo3d<sub>i</sub>) represents the MoS<sub>2</sub> domains on SiO<sub>2</sub>/Si next to the WSe<sub>2</sub> crystal (Mo3d<sub>5/2</sub>, BE = 229.90 eV), with a size of about 4 μm. The binding energy is very close to what is reported for bulk, pristine

MoS<sub>2</sub> (229.7 eV). The second group are distinct spectra-at-pixels from one of the VHS to the bottom of the WSe<sub>2</sub> crystal, with BE = 230.10 eV (Mo3d<sub>II</sub>). The third group represents another type of VHS sitting closer to the center with BE = 230.26 eV (Mo3d<sub>III</sub>). The weak energy shift cannot be explained by major chemical changes, such as oxidation, because oxygen is absent in the VHS regions according to the map of Fig. 3(a). The Mo/S ratio as seen from the Mo3d and S2s maps of Fig. 3(c) is also very similar and confirmed by the extracted values. Rather, it is assumed that the observed, faint positive energy shift observed in the VHS (unlike the one for the MoS<sub>2</sub> domain on SiO<sub>2</sub>/Si) is due to different charge transfer behaviors in MoS<sub>2</sub> sitting on WSe<sub>2</sub>. Higher binding energies are consistent with charge transfer from WSe<sub>2</sub> to MoS<sub>2</sub> due to the more pronounced *n*-type character of WSe<sub>2</sub>. Thus, upon transfer onto WSe<sub>2</sub>, monolayer MoS<sub>2</sub> becomes more *n*-type, but to a different extent depending on whether type II or type III domains are considered according to the binding shifts summarized in Table I. We explain this difference by the quality of the initial WSe<sub>2</sub> crystal, as can be seen from the PEEM image of Fig. 2; indeed, it seems that domain II contains larger amount of open cracks, thereby leading to less *n*-doping by WSe<sub>2</sub>.

### D. Correlation of the chemistry with electronic properties

The electronic properties of the sample at the micrometer scale were studied by two means: mapping out the local work function and recording spatially resolved band structure data. We consider first the work function values determined from fitting of the secondary-electron threshold according to a method described elsewhere, with a sensitivity of 25 meV. From the work function map<sup>23</sup> presented in Fig. 6, we can first determine the WSe<sub>2</sub> WF to be 4.50 eV. Second, we measure the MoS<sub>2</sub> WF on WSe<sub>2</sub> (VHS region) and see that it is a slightly but significantly lower (4.7 eV) value than the one for MoS<sub>2</sub>/SiO<sub>2</sub> (4.74 eV). This is consistent with the observed contact potential difference of the two regions based on Kelvin-force

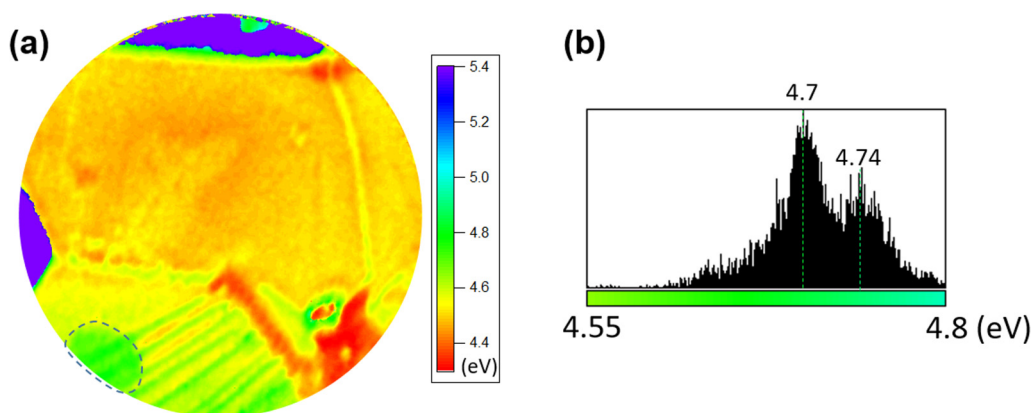


**FIG. 6.** (a) WF map of the area containing MoS<sub>2</sub>/WSe<sub>2</sub> VHS (yellow dashed circle in Fig. 1) on SiO<sub>2</sub>/Si; (b) work function distribution of MoS<sub>2</sub> on WSe<sub>2</sub> based on the WF map [(dashed area in (a))].

21 January 2025 15:25:16

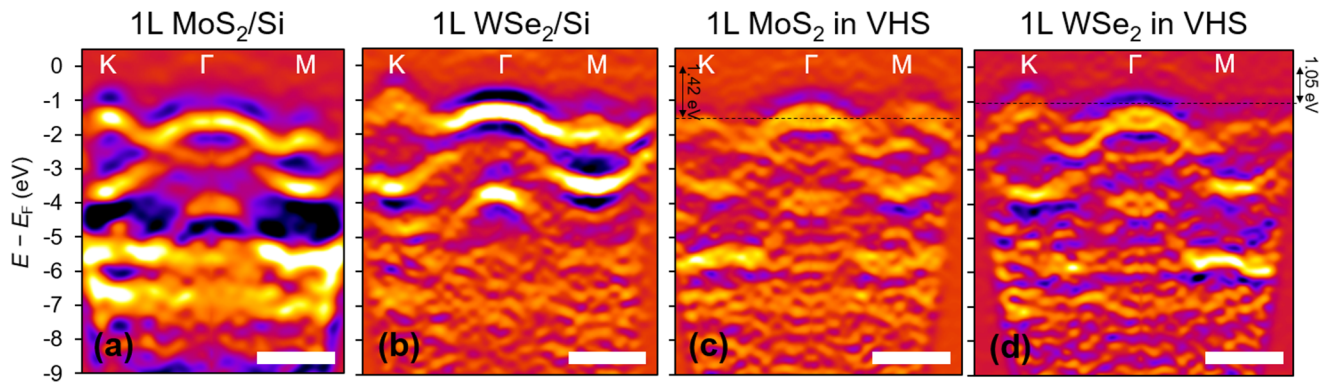


**FIG. 7.** (a) Valence band structure of (a) MoS<sub>2</sub>/SiO<sub>2</sub>/Si, (b) WSe<sub>2</sub>/SiO<sub>2</sub>/Si, (c) MoS<sub>2</sub>/WSe<sub>2</sub>/SiO<sub>2</sub>/Si VHS along high-symmetry points of MoS<sub>2</sub>, and (d) MoS<sub>2</sub>/WSe<sub>2</sub>/SiO<sub>2</sub>/Si VHS along high-symmetry points of WSe<sub>2</sub>. The scale bar represents 1 Å<sup>-1</sup> in k-space along the x axis direction. Second derivative filter was applied to enhance the contrast of the bands. Note that at the  $\Gamma$  point, valence band structures of MoS<sub>2</sub> and WSe<sub>2</sub> are overlapped.

microscopy (KFM) images (see the supplementary material for the KFM results)<sup>39</sup> as well as the binding energy shift observed in the Mo core level in Fig. 5.

Figure 7 shows the valence band structures of individual layers and VHS obtained by kPEEM and recorded over a typical area diameter of 15  $\mu\text{m}$  (defined as the size of the field aperture of the PEEM used for area selection). From Figs. 7(a) and 7(b), we observe the ML-character of the MoS<sub>2</sub> and WSe<sub>2</sub> crystals from the upward shift of the K-bands getting closer to the Fermi level than the  $\Gamma$ -bands ( $\Delta E_{\Gamma-K}$  being measured at approximately 240 and 400 meV, respectively, for MoS<sub>2</sub> and WSe<sub>2</sub> in agreement with literature data). Also, in the case of WSe<sub>2</sub>, the expected larger energy separation of the valence band maximum at  $\Gamma$  and K due to the larger spin-orbit splitting is evident. For the VHS band structure images [Figs. 7(c) and 7(d)], the high-symmetry points for each TMD were determined from constant-energy kPEEM image series from the same acquisition. Careful inspection of the individual kPEEM images of the VHS enables us to identify the weaker fingerprint of the MoS<sub>2</sub> K-bands, hence allowing us to obtain layer-specific band structures thanks to a cut along the corresponding high-symmetry points [Figs. 7(c) and 7(d)]. Besides, we can determine the in-plane orientation of both MoS<sub>2</sub> and WSe<sub>2</sub> crystals. This yields a lattice orientation of 15.7° with respect to each other. It is evident also from the valence band positions of MoS<sub>2</sub> on Si and MoS<sub>2</sub> on WSe<sub>2</sub> that MoS<sub>2</sub> VBM at the K point is farther away from the Fermi level for VHS, again indicating that MoS<sub>2</sub> supported by WSe<sub>2</sub> exhibits *n*-type doping. This is in agreement with the core-level binding energies reported in Table I. Previously it was reported that MoS<sub>2</sub>, naturally an *n*-type semiconductor, becomes more *p*-doped when it is in contact with WSe<sub>2</sub>.<sup>24,25</sup> In our case, the opposite trend is observed. This is to be likely the result of several factors, such as differences in initial electron affinity (where the WSe<sub>2</sub> work function appears to be much less than that of MoS<sub>2</sub>), interaction with the silicon substrate, interfacial polymer residues from the transfer methods, or lattice orientation dependent

interlayer interaction.<sup>25–33</sup> Based on the work function mapping, the valence band offset determined from the valence band maximum of the individual layers in the heterostructure from Figs. 7(c) and 7(d), and using reported values for the electronic bandgaps,<sup>25,34–38</sup> we have constructed the band alignment diagram of the MoS<sub>2</sub>/WSe<sub>2</sub> VHS (Fig. 8). This yields a type II heterostructure as expected from the WSe<sub>2</sub>/MoS<sub>2</sub> band diagram<sup>25</sup> but with a very small conduction-band offset of  $\sim 0.04$  eV, which may have an important implication in understanding and exploiting the optoelectronic behavior of the heterostructure.

The photoluminescence spectroscopy of the same MoS<sub>2</sub> island on SiO<sub>2</sub> (270 nm)/Si and WSe<sub>2</sub>/SiO<sub>2</sub>/Si (Fig. 9) also corroborates that MoS<sub>2</sub>/WSe<sub>2</sub> VHS forms a type II heterostructure with a very small conduction-band offset. The photoluminescence intensity of both WSe<sub>2</sub> and MoS<sub>2</sub> layers was suppressed in the case of the VHS. This is likely due to the additional doping and efficient transfer of the carriers at the conduction-band edges leading to more significant non-radiative recombination channels.

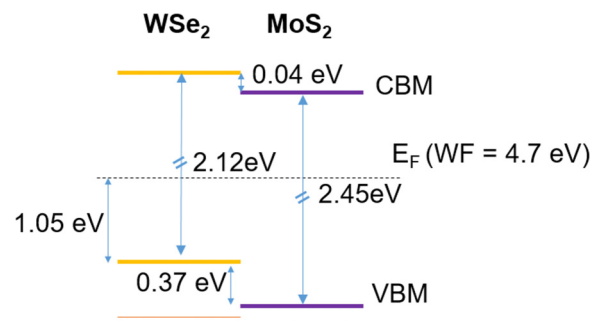


**FIG. 8.** Band alignment diagram of the MoS<sub>2</sub>/WSe<sub>2</sub> heterostructure. Electronic bandgaps of monolayer MoS<sub>2</sub> and WSe<sub>2</sub>, as reported previously (Refs. 36–38), were estimated from known experimental values.

21 January 2025 15:25:16

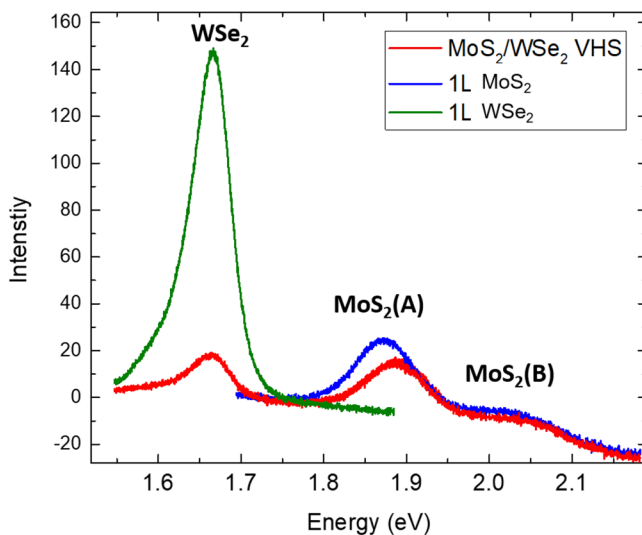


FIG. 9. Photoluminescence spectra in the excitonic ranges of WSe<sub>2</sub> (exciton A) and MoS<sub>2</sub> (exciton A and B) from 1L MoS<sub>2</sub>, 1L WSe<sub>2</sub>, and VHS areas.

#### IV. SUMMARY AND CONCLUSIONS

We have shown a quantitative correlation between chemical and electronic states in single layer WSe<sub>2</sub>, MoS<sub>2</sub>, and related vertical heterostructures by using photoelectron emission microscopy at the laboratory scale enabling elemental, work function, and band structure mapping over the same areas. Laterally resolved chemical fingerprinting from pixel-by-pixel data reduction of core-level images using efficient postprocessing techniques can be achieved at an unprecedented level of accuracy. For monolayer MoS<sub>2</sub>, the method reveals substrate-dependent charge transfer properties within the narrow energy range of 360 meV, with MoS<sub>2</sub> becoming more *n*-type in VHS. The band structure data from momentum microscopy taken over the same areas confirm the charge transfer from WSe<sub>2</sub> to MoS<sub>2</sub> by the shift of the K-bands away from the Fermi level and show layer-specific contributions to the electronic band structure of the VHS. From the work function and momentum microscopy results, the energy-level diagram is reconstructed revealing a type II heterostructure, but with a very small conduction-band offset. This study highlights the importance of combining all possible photoemission spectral fingerprints with lateral and energy resolution in a quantitative way to achieve a unified understanding of 2D material heterostructures.

#### ACKNOWLEDGMENTS

This work, carried out on the Platform for Nanocharacterisation (PFNC), was supported by the “Recherche Technologique de Base” program of the French National Research Agency (ANR). Chuck Fadley led our field of photoelectron spectroscopy over more than 50 years. His enthusiasm and curiosity for novel photoemission techniques and his outstanding scientific

career (not mentioning his great sense of humor) will remain in our memory.

#### DATA AVAILABILITY

The data that support the findings of this study are available from the corresponding author upon reasonable request.

#### REFERENCES

- <sup>1</sup>M. Amati *et al.*, *J. Electron Spectrosc. Relat. Phenom.* **224**, 59 (2018).
- <sup>2</sup>L. Gregoratti, T. O. Menten, A. Locatelli, and M. Kiskinova, *J. Electron Spectrosc. Relat. Phenom.* **170**, 13 (2009).
- <sup>3</sup>S. Ulstrup *et al.*, *ACS Nano* **10**, 10058 (2016).
- <sup>4</sup>M. T. Dau *et al.*, *Appl. Phys. Lett.* **110**, 011909 (2017).
- <sup>5</sup>D.-J. Yun *et al.*, *2D Mater.* **7**, 025002 (2020).
- <sup>6</sup>C. Mathieu, N. Barrett, J. Rault, Y.-Y. Mi, B. Zhang, W. A. de Heer, C. Berger, E. H. Conrad, and O. Renault, *Phys. Rev. B* **83**, 235436 (2011).
- <sup>7</sup>M. T. Dau *et al.*, *ACS Nano* **12**, 2319 (2018).
- <sup>8</sup>M. Frégnaux, H. Kim, D. Rouchon, V. Derycke, J. Bleuse, D. Voiry, M. Chhowalla, and O. Renault, *Surf. Interface Anal.* **48**, 465 (2015).
- <sup>9</sup>O. Renault, M. Lavayssière, A. Bailly, D. Mariolle, and N. Barrett, *J. Electron Spectrosc. Relat. Phenom.* **171**, 68 (2009).
- <sup>10</sup>D. Dumcenco *et al.*, *ACS Nano* **9**, 4611 (2015).
- <sup>11</sup>H. Kim, D. Ovchinnikov, D. Deiana, D. Unuchek, and A. Kis, *Nano Lett.* **17**, 5056 (2017).
- <sup>12</sup>S. Li *et al.*, *Nat. Mater.* **17**, 535 (2018).
- <sup>13</sup>S. Bertolazzi, D. Krasnozhan, and A. Kis, *ACS Nano* **7**, 3246 (2013).
- <sup>14</sup>M. Escher, K. Winkler, O. Renault, and N. Barrett, *J. Electron Spectrosc. Relat. Phenom.* **178**, 303 (2010).
- <sup>15</sup>O. Renault, *Surf. Interface Anal.* **42**, 816 (2010).
- <sup>16</sup>In this mode, electrons impinge first onto the image intensifier and create a short light flash. A fast CDD camera images these light flashes and an analog image is created and transferred to the frame grabber card. Then, the computer analyses the images with the event-counting algorithm and converts them to digital images, where a single event is represented by exactly one grayscale; a present number of images is accumulated during the dwell time of the detector. Finally, the accumulated event image is displayed in the imaging software.
- <sup>17</sup>W. C. Jin *et al.*, *Phys. Rev. Lett.* **111**, 106801 (2013).
- <sup>18</sup>M. Lavayssière, M. Escher, O. Renault, D. Mariolle, and N. Barrett, *J. Electron Spectrosc. Relat. Phenom.* **186**, 30 (2013).
- <sup>19</sup>M. P. Seah, *Surf. Interface Anal.* **33**, 950 (2002).
- <sup>20</sup>O. Renault, A. Garnier, J. Morin, N. Gambacorti, and F. Bertin, *Appl. Surf. Sci.* **258**, 10077 (2012).
- <sup>21</sup>V. Fernandez, O. Renault, and N. Fairley, “Optimising XPS Instrument Performance for Quantification of Spectra” (submitted) (2020).
- <sup>22</sup>S. Tanuma, C. J. Powell, and D. R. Penn, *Surf. Interface Anal.* **21**, 165 (1994).
- <sup>23</sup>O. Renault, R. Brochier, A. Roule, P.-H. Haumesser, B. Krömker, and D. Funnemann, *Surf. Interface Anal.* **38**, 375 (2006).
- <sup>24</sup>R. Cheng *et al.*, *Nano Lett.* **14**, 5590 (2014).
- <sup>25</sup>S. Latini, K. T. Winther, T. Olsen, and K. S. Thygesen, *Nano Lett.* **17**, 938 (2017).
- <sup>26</sup>D. Unuchek, A. Ciarrocchi, A. Avsar, K. Watanabe, T. Taniguchi, and A. Kis, *Nature* **560**, 340 (2018).
- <sup>27</sup>M.-H. Chiu *et al.*, *Nat. Commun.* **6**, 7666 (2015).
- <sup>28</sup>C. Li, X. Yan, X. Song, W. Bao, S. Ding, D. W. Zhang, and P. Zhou, *Nanotechnology* **28**, 415201 (2017).
- <sup>29</sup>H. Terrones, F. López-Urías, and M. Terrones, *Sci. Rep.* **3**, 1549 (2013).
- <sup>30</sup>M. M. Ugeda *et al.*, *Nat. Mater.* **13**, 1091 (2014).
- <sup>31</sup>J. H. Park *et al.*, *ACS Nano* **13**, 7545 (2019).
- <sup>32</sup>W. Zhao *et al.*, *Nano Res.* **12**, 3095 (2019).
- <sup>33</sup>J. Kunstmann *et al.*, *Nat. Phys.* **14**, 801 (2018).

21 January 2025 15:25:16

<sup>34</sup>P. S. Schmidt, C. E. Patrick, and K. S. Thygesen, *Phys. Rev. B* **96**, 205206 (2017).

<sup>35</sup>F. A. Rasmussen and K. S. Thygesen, *J. Phys. Chem. C* **119**, 13169 (2015).

<sup>36</sup>Y. L. Huang *et al.*, *Nat. Commun.* **6**, 6298 (2015).

<sup>37</sup>A. R. Klots *et al.*, *Sci. Rep.* **4**, 66078 (2014).

<sup>38</sup>C. Zhang, Y. Chen, A. Johnson, M. Y. Li, L. J. Li, P. C. Mende, R. M. Feenstra, and C. K. Shih, *Nano Lett.* **15**, 6494 (2015).

<sup>39</sup>See the supplementary material at <https://www.scitation.org/doi/suppl/10.1116/6.0001135> for Kelvin-Force Microscopy measurements.